Supporting Information for: Fully-Connected Microwave Photonic Multi-Beamformer with Fast Beam-Steering for Broadband Wireless Communication

Author Information

Ziheng Ni[1], Liangjun Lu[1,2,*], Kai Fu[1], Haowei Zhang[1], Jianping Chen[1,2] and Linjie Zhou[1,2,*]

[1]State Key Laboratory of Photonics and Communications, Department of Electronic Engineering, Shanghai Jiao Tong University, Shanghai 200240, China.

[2]SJTU-Pinghu Institute of Intelligent Optoelectronics, Pinghu 314200, China

e-mail: luliangjun@sjtu.edu.cn, ljzhou@sjtu.edu.cn

Contents

S1. Theoretical performance of fully-connected and partially-connected architectures

In a fully-connected (FC) architecture, each RF chain is connected to all M antenna elements. When transmitting a single beam, the signal from one RF chain is distributed across the entire array, enabling coherent combination from all antennas. In a partially-connected (PC) architecture, the array is divided into N disjoint subarrays, each driven by one RF chain. When transmitting a single beam, only the antennas within the corresponding subarray contribute, so each beam uses M/N antennas. This structural difference leads to higher per-beam coherent gain in FC, but also to greater hardware complexity and insertion loss.

We consider an array of M antenna elements transmitting N simultaneous beams, each supported by one RF chain. Let $b \in \{1,2,\ldots,N\}$ denote the beam index, corresponding to the b-th intended transmission direction (or equivalently, the b-th user). Each beam is allocated the same transmit power P_{RF}, so that the total radiated power is equal in both architectures, $P_{tot} = NP_{RF}$. The steering vector toward direction θ_b is denoted by $\boldsymbol{a}(\theta_b) \in C^M$, describing the relative phases across antenna elements. For a uniformly weighted array with isotropic elements, we normalize as

$$\|\boldsymbol{a}(\theta_b)\|_2^2 = M. \tag{1}$$

The transmit weight vector for beam b is $\boldsymbol{w}_b \in C^M$, satisfying the power constraint

$$\|\boldsymbol{w}_b\|_2^2 = P_{RF}. \tag{2}$$

The ideal directional (array) gain is defined as

$$G_b = \frac{|a^H(\theta_b)\boldsymbol{w}_b|^2}{\|\boldsymbol{w}_b\|_2^2}. \tag{3}$$

which quantifies the coherent amplification relative to isotropic transmission. To account for hardware non-idealities (splitter/combiner loss, phase-shifter loss, calibration errors), we introduce an efficiency factor $\eta_b \in (0, 1]$. The effective gain is then

$$G_{b,eff} = \eta_b G_b \tag{4}$$

In the FC architecture, each RF chain is connected to all M antenna elements. With phase-conjugate, equal-gain transmission, the maximum effective gain is

$$\mathrm{G}_{b,eff}^{FC} = \eta_b^{FC} M. \tag{5}$$

In the PC architecture, the array is divided into N disjoint subarrays, each of size M/N, driven by one RF chain. With the same design within each subarray, the effective gain is

$$\mathrm{G}_{b,eff}^{PC} = \eta_b^{PC} \frac{M}{N}. \tag{6}$$

The gain ratio is

$$\frac{G_{b,eff}^{FC}}{G_{b,eff}^{PC}} = \frac{\eta_b^{FC}}{\eta_b^{PC}} N. \quad (7)$$

Thus, FC achieves up to an N-fold per-beam advantage only if hardware efficiencies are comparable ($\eta_b^{FC} \approx \eta_b^{PC}$). Otherwise, the practical advantage is reduced by the efficiency ratio. In a single-path propagation scenario aligned with the intended beam, the receive *SNR* is

$$SNR_b \propto \frac{P_{RF} G_{b,eff}}{\sigma^2}, \quad (8)$$

where σ^2 is the receiver noise power. The SNR ratio then becomes

$$SNR_b^{FC} : SNR_b^{PC} = \frac{\eta_b^{FC}}{\eta_b^{PC}} N : 1. \quad (9)$$

In conclusion, the *N*-fold gain/SNR improvement holds only when hardware efficiencies are similar. Nevertheless, as the number of beams (*N*) increases, the relative advantage of FC over PC generally improves, provided efficiency does not degrade sharply.

S2. Design of the optical true time delay line (OTTDL)

Supplementary Figure 1a illustrates the structural design of a single-stage delay unit, which serves as the fundamental building block of the reconfigurable optical delay line. This unit integrates several essential photonic components to achieve precise temporal control of optical signals. At its core is a Mach – Zehnder interferometer (MZI)-based electro-optic (EO) switch that enables dynamic routing the optical signal by modulating the phase difference between its two arms, allowing for controlled selection between different delay paths with minimal insertion loss and crosstalk. To address the finite extinction ratio of the EO switch, a variable optical attenuator (VOA) is introduced in each unit to suppress residual light leakage into unintended paths. This attenuation mechanism compensates for imperfect switching isolation, thereby preserving the integrity of the temporal response and reducing spurious signal components. The delay values are defined by ridge waveguides of varying lengths, which generate discrete delay intervals. This approach, which relies solely on the length differences of long straight ridge waveguides to implement delay, minimizes the calculated delay errors between the two arms. To further improve the delay accuracy and minimize the loss caused by mode-field mismatching at curved sections, the design incorporates widened Euler bend waveguides in curved regions. The Euler bend geometry reduces mode mismatch in the bending region, thereby lowering bending loss, while also enabling a more compact footprint compared to conventional bend waveguides. In addition, local widening of the waveguide suppresses scattering loss by reducing the modal overlap with the waveguide sidewalls. This compact and modular structure enables scalable and low-error delay synthesis, which is essential for high-speed photonic signal processing and time-domain multiplexing systems.

The delay waveguides in the OTTDL chip are implemented using 2-μm-wide ridge waveguides, which feature a 90-nm-thick slab and a total waveguide thickness of 220 nm. Supplementary Figure 1b shows the cross-section of the 2-μm-wide ridge delay waveguide, while Supplementary Fig. 1c shows the cross-section of the PIN-diode-based VOA integrated into each stage of the delay lines. The diode is controlled through two metal layers (Metal 1 and Metal 2), positioned on top of the oxide cladding. The structure allows for precise tuning of the optical signal attenuation by modulating the bias voltage applied across the diode, thereby varying the optical absorption in the waveguide.

Supplementary Fig. 1| a Structural design of a single-stage delay unit. **b** Cross-section of the 2-μm-wide ridge waveguide. **c** Cross-section of the PIN-diode-based VOA.

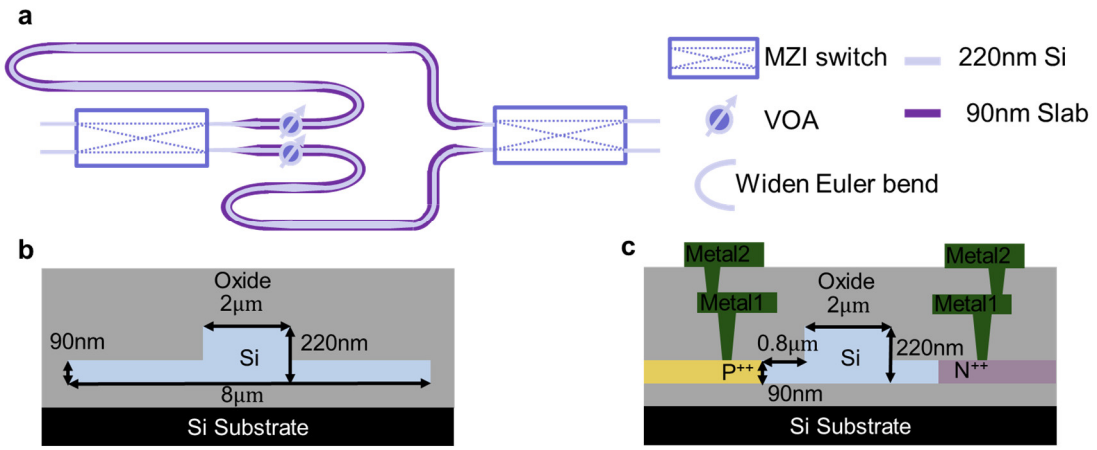

Supplementary Figure 2a illustrates the simulated waveguide group index deviation of a 500-nm strip waveguide and a 2-μm-wide ridge waveguide under waveguide width variation. The simulation results indicate that for the 2 μm-wide ridge waveguide, the group index variation of the fundamental mode remains as low as ~0.003, even when the waveguide width deviates by ±60 nm from its nominal value. In contrast, the 500 nm-wide strip waveguide exhibits a much larger group index variation of ~0.46 under the same width deviation, highlighting a fabrication tolerance improvement of more than two orders of magnitude. For a delay segment designed to generate a total delay of 310.59 ps, this corresponds to a delay error of only ~0.42 ps by using the 2 μm ridge waveguide, compared to ~64.4 ps with the 500 nm strip waveguide—resulting in an approximately 150× reduction in delay uncertainty. Moreover, as shown in Supplementary Fig. 1a, the delay is implemented exclusively through the length differences of 2 μm-wide straight ridge waveguides, which helps to further suppress bending-induced dispersion and enhance the overall delay accuracy. The broad ridge geometry also reduces the modal overlap with waveguide sidewalls, thereby minimizing scattering loss induced by sidewall roughness. As a result, this waveguide design simultaneously achieves high delay precision and low optical loss, which are critical for scalable and high-performance photonic beamforming networks.

Furthermore, Supplementary Figure 2b also shows the simulated transmission spectra of the 2×2 multimode interference (MMI) coupler used in the MZI switch. The simulation indicates an insertion loss of approximately 0.09 dB at 1550 nm, with a minimum value of 0.075 dB at 1560 nm. Across the full wavelength range from 1520 nm to 1580 nm, the simulated insertion loss remains below 0.17 dB, confirming the low-loss and broadband performance of the MMI coupler.

Supplementary Fig. 2| a Simulated group index deviation of a 500-nm-wide strip waveguide and a 2-μm-wide ridge waveguide under waveguide width variation. b Simulated transmission of the 2×2 MMI.

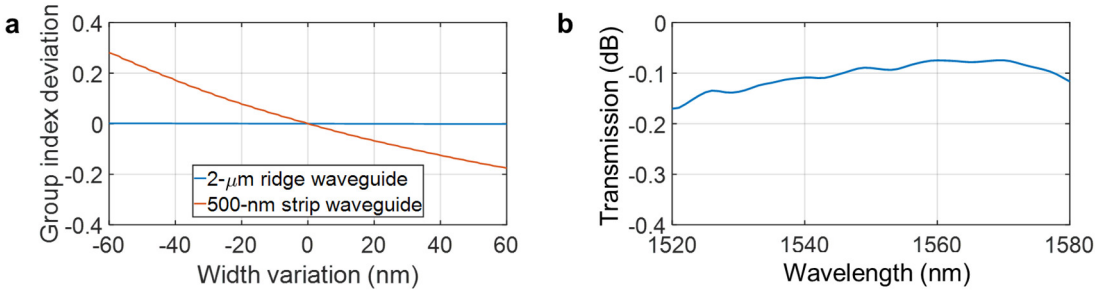
a
Group index deviation
0.4
0.2
0
-0.2
-0.4
-60
-40
-20
0
20
40
60
Width variation (nm)
2-μm ridge waveguide
500-nm strip waveguide
b
Transmission (dB)
0
-0.1
-0.2
-0.3
-0.4
1520
1540
1560
1580
Wavelength (nm)

S3. Experimental results of the components in the OTTDL

Supplementary Figures 3a presents the wafer-level test results of average propagation losses across the 1520-1580 nm wavelength range of 2-μm-wide ridge waveguides in the 8-inch SOI wafer. The propagation loss of the 2-μm-wide ridge delay waveguides, measured using the cut-back method, is below 0.22 dB/cm for all 26 measured dies. It exhibits an average loss of approximately 0.15 dB/cm. Supplementary Figure 3b illustrates the deviation of the measured group delay per unit length (ps/cm) of the 2-μm-wide ridge delay waveguides from the simulated value for all 26 dies. The measured average delay is 124.4950 ps/cm, and the deviation across all dies does not exceed 0.19 ps/cm, indicating highly consistent delay performance and minimal process-induced variation. These results confirm that the wide ridge waveguide demonstrates low group delay variation and excellent fabrication tolerance. Furthermore, by combining the results from Supplementary Figures 3a and 3b, the loss per unit delay can be calculated as 0.15 dB/cm ÷ 124.4950 ps/cm = 1.205 dB/ns, confirming the low-loss characteristic of the delay line.

Supplementary Figures 3c show the average insertion loss of the 2×2 MMIs across the 1520-1580 nm wavelength range of all 26 dies in the wafer. The loss of the 2×2 MMIs was extracted by measuring cascaded MMI structures. Most of the MMIs demonstrate an average insertion loss of less than 0.18 dB across the 60 nm wavelength span, further supporting the low-loss and high-yield characteristics of our passive components.

Supplementary Fig. 3| Wafer-level test results. **a** Average propagation loss of the 2-μm-wide ridge waveguides (dB/cm). **b** Deviation of the measured group delay per unit length from the simulated value (ps/cm). **c** Average insertion loss of the MMIs (dB).

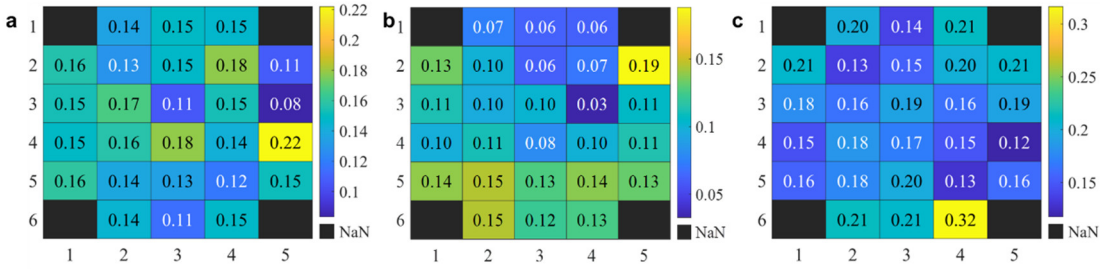

Supplementary Figure 4a shows the measured transmission of the MZI switch under various applied voltages to the EO phase shifters, while the TO phase shifter is pre-calibrated to the quadrature operation point. The EO switching voltages for the cross and the bar states are both close to 0.96V. Both states exhibit extinction ratios > 25 dB, outperforming traditional silicon EO switches by tuning only one phase shifter. Furthermore, we measured the temporal response of the switch by applying an electrical square-wave signal with a frequency of 1 MHz to one of the PIN phase shifters. The modulated optical signal was received by a PD and recorded by an oscilloscope (OSC). Supplementary Figure 4b shows the measured waveforms

of the applied electrical signal and the received optical signal. The 10%-90% rise and fall time of the switch is 8 and 15 ns, respectively, which verifies the high switching operation capability of our OTTDLs. Supplementary Figures 4c and 4d depict the measured transmission spectra of the electro-optic switch integrated within the delay line at the bar and cross states, respectively. The insertion loss is 0.79/0.95 dB at the bar/cross state at the 1550 nm wavelength. The crosstalk is -25.24 dB at the bar state and -25.18 dB at the cross state. The consistent performance across 1520-1580 nm highlights the effectiveness of the electro-optic switch within the delay line architecture, ensuring reliable signal routing with minimal degradation.

Supplementary Fig. 4| Performance of EO switch. a Measured output optical power of the switch unit with various voltages applied to the EO phase shifters. **b** Switching time of the switch unit. **c** Measured transmission spectra of the switch element at the bar state. **d** Measured transmission spectra of the switch element at the cross state.

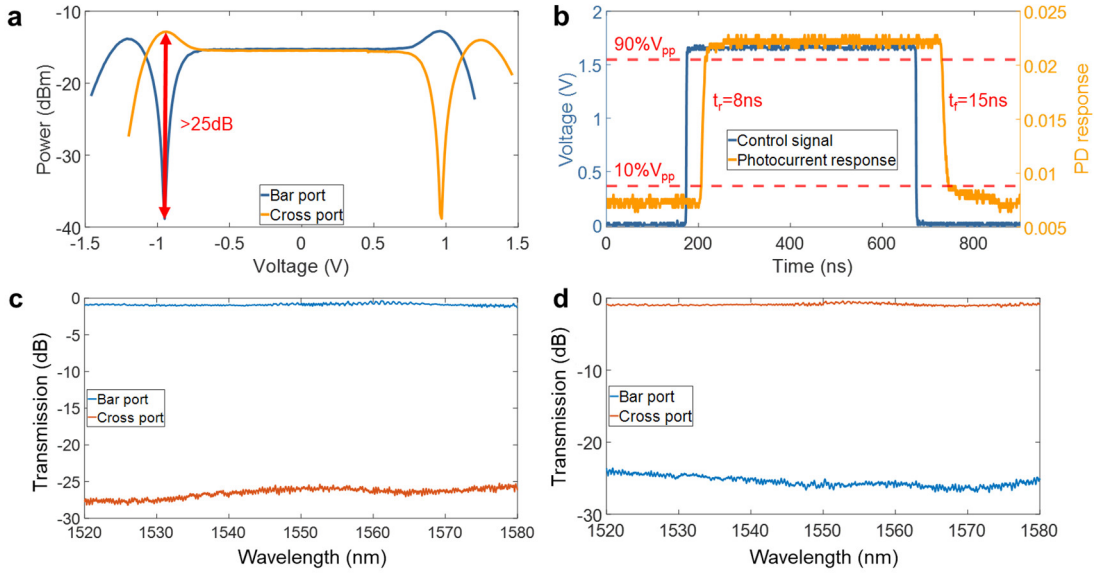

S4. Additional information for experimental setups

Supplementary Figure 5 provides an overview of the experimental setups used to assess various aspects of the OTTDL chip. Supplementary Figure 5a illustrates the optical transmission measurement system, which employs a tunable laser, a polarization controller, and an optical power meter to evaluate the insertion loss and transmission spectra across all channels and delay states. Supplementary Figure 5b depicts the setup for switching time measurement of the OTTDL, where an oscilloscope and control pulse synchronization are used to quantify the reconfiguration dynamics. Supplementary Figure 5c presents the electrical S21 measurement setup, powered by a vector network analyzer (VNA), to meticulously characterize amplitude and phase responses and derive group delay spectra. Supplementary Figure 5d shows the experimental configuration of the receiver side of a microwave photonic multi-beam wireless communication system. In this setup, the optical signals processed by the fully-connected beamforming network were received by a phased-array antenna and converted to electrical signals, enabling the evaluation of beamforming performance and signal quality under realistic wireless conditions.

Supplementary Fig. 5| a Setup for measuring the optical transmission spectrum using a tunable laser source (TLS). **b** Experimental setup for measuring the response time of the OTTDL. **c** Setup for measuring the RF transmission coefficient (S21) using a VNA. **d** Experimental setup of the receiver module for wireless transmission. DUT: device under test; EDFA: erbium-doped fiber amplifier; OSC: oscilloscope; LNA: low-noise amplifier; ESA: electrical spectrum analyzer.

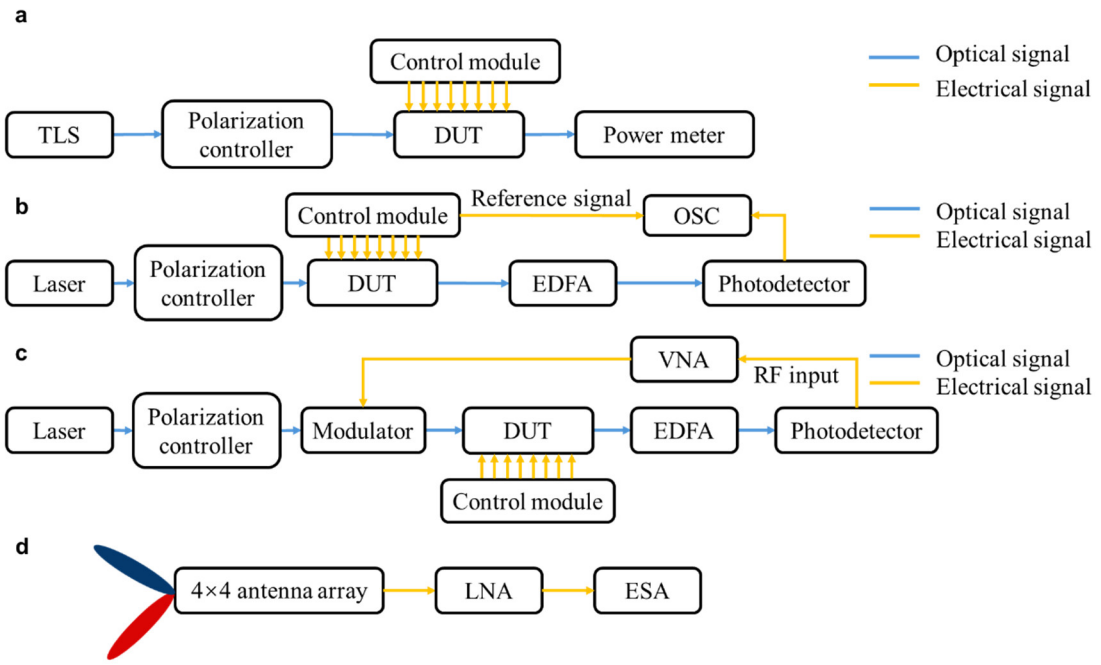

S5. Additional results for OTTDLs

Supplementary Fig. 6| a-h Measured transmission spectra of Channel 1-8.

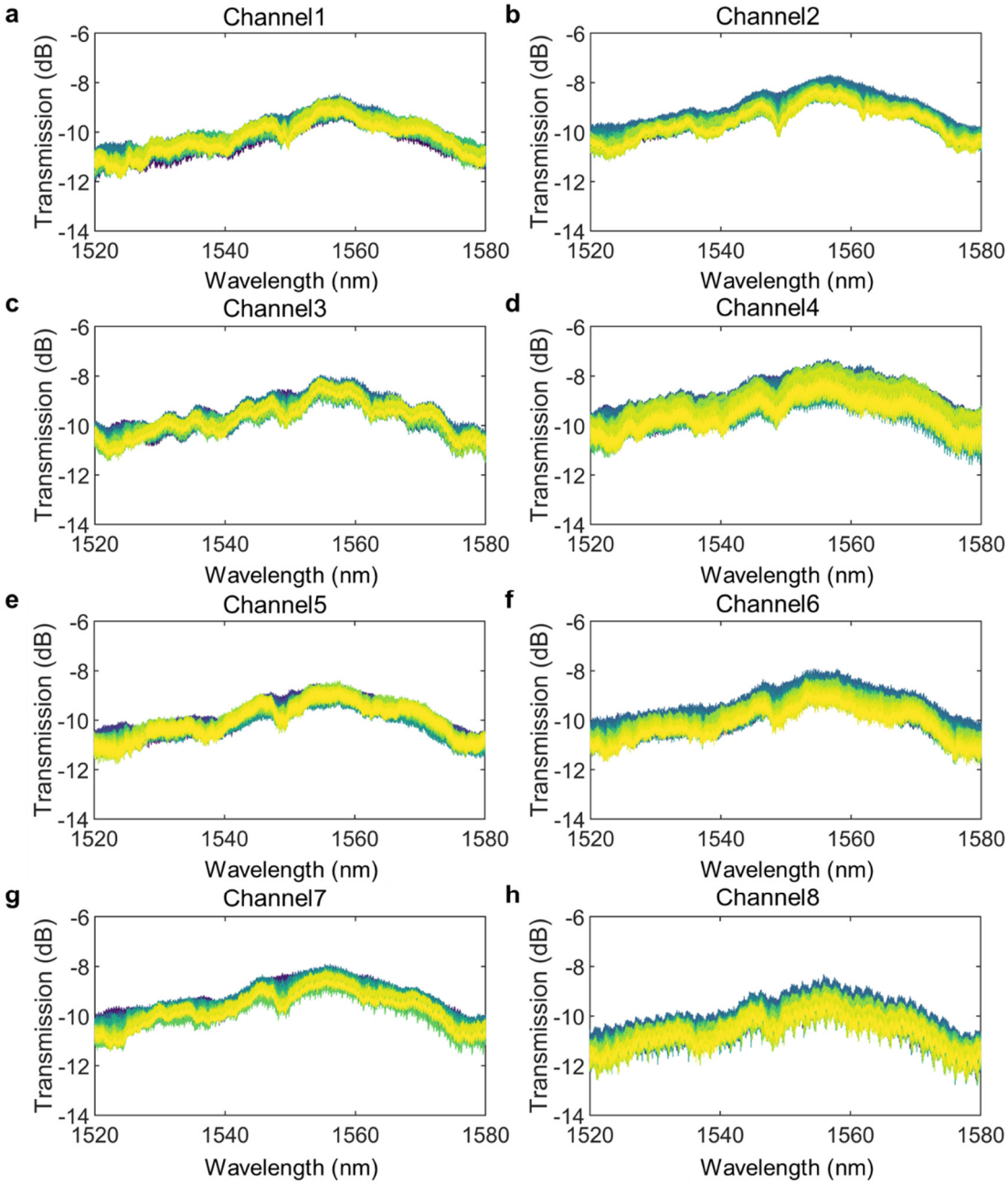

The measured transmission spectra of the 8-channel OTTDL chip are shown in Supplementary Figure 6, where each panel corresponds to one of the 8 channels, and each channel consists of 64 different delay states. Importantly, across all 64 delay states of each channel, the total insertion loss measured at the 1555 nm wavelength—including fiber-to-chip coupling loss—remains below 10 dB, demonstrating the low-loss performance of the delay line across its full reconfiguration range. Moreover, the spectral envelope of the delay line is closely related to that of the MMI-based loss spectrum, with the regions of higher loss in the measured transmission spectra coinciding well with those predicted in the MMI simulation results.

Supplementary Figure 7 presents the S21 measurements for the 8-channel delay line, with each channel exhibiting 64 distinct delay states. In each subplot, the different colored curves represent the transmission spectra for various delay states within the respective channel.

Supplementary Fig. 7| a-h Measured S21 of Channel 1-8.

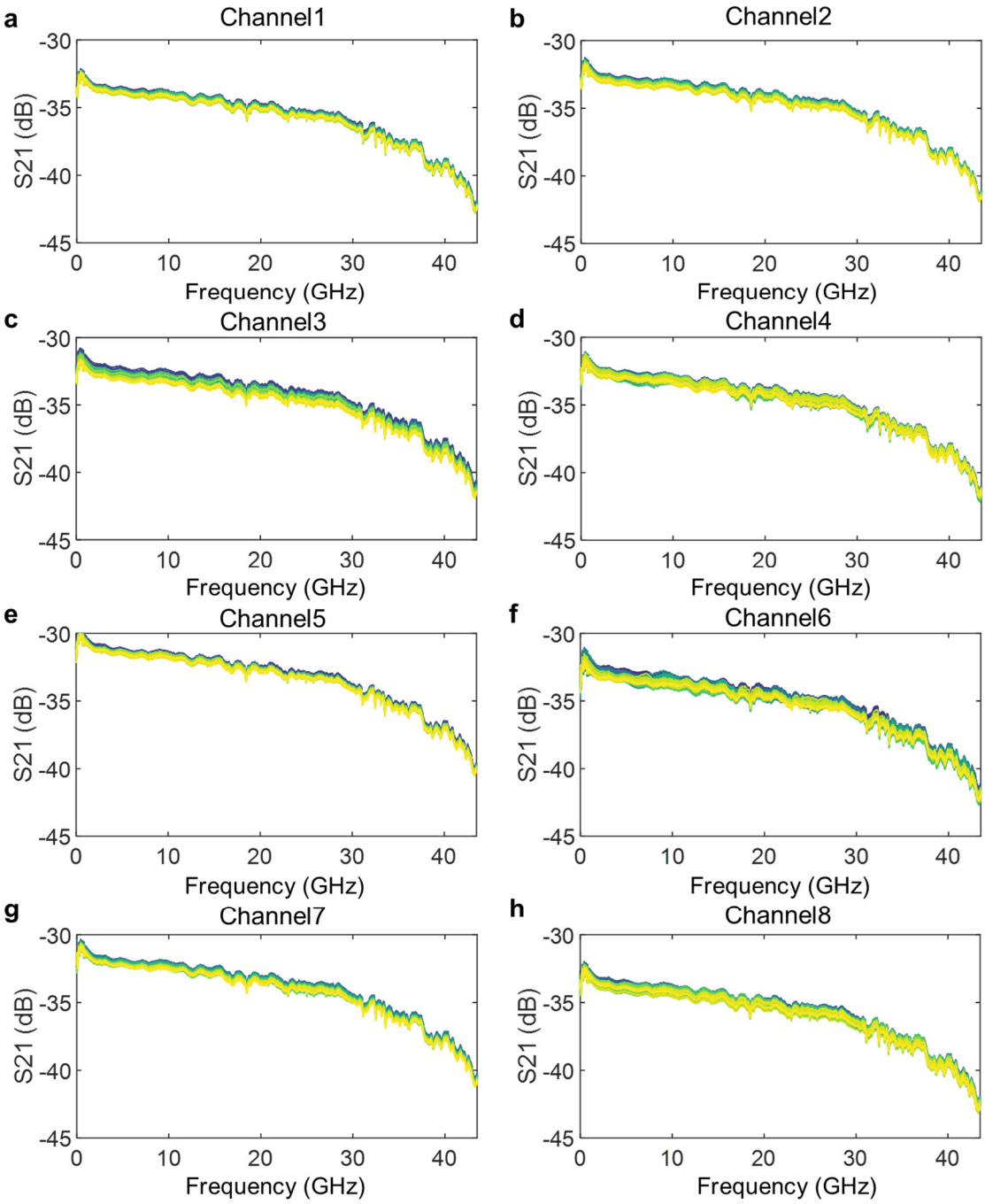

The measured phase responses for 64 delay states of all 8 channels are shown in Supplementary Fig. 8, with the phase delay normalized to the shortest delay state in each channel, illustrating the variation of S21 phase with frequency.

Supplementary Fig. 8| a-h Measured phase of Channel 1-8.

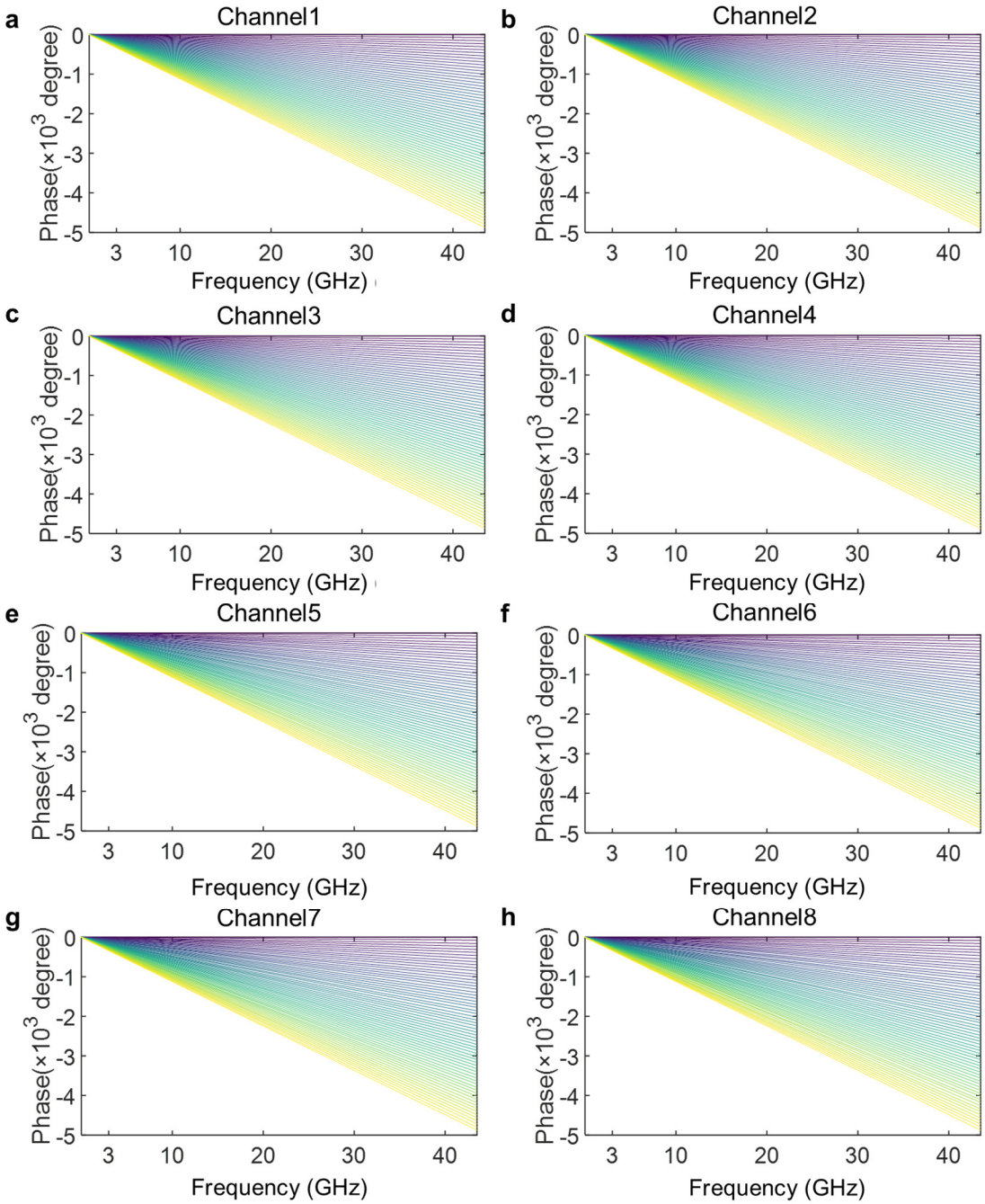

Supplementary Figure 9 presents the measured group delay spectra of the chip, with each channel supporting 64 distinct delay states. In each subplot, a series of 64 traces corresponds to the different delay configurations within that specific channel. The measured results demonstrate that, across all channels, the group delay remains stable over the full operating bandwidth, with each delay state yielding a nearly flat response across frequency. This indicates that the delay line provides true-time delay behavior rather than phase shifting, thereby eliminating beam squint in the wideband beamforming applications.

Supplementary Fig. 9| a-h Measured delay of Channel 1-8.

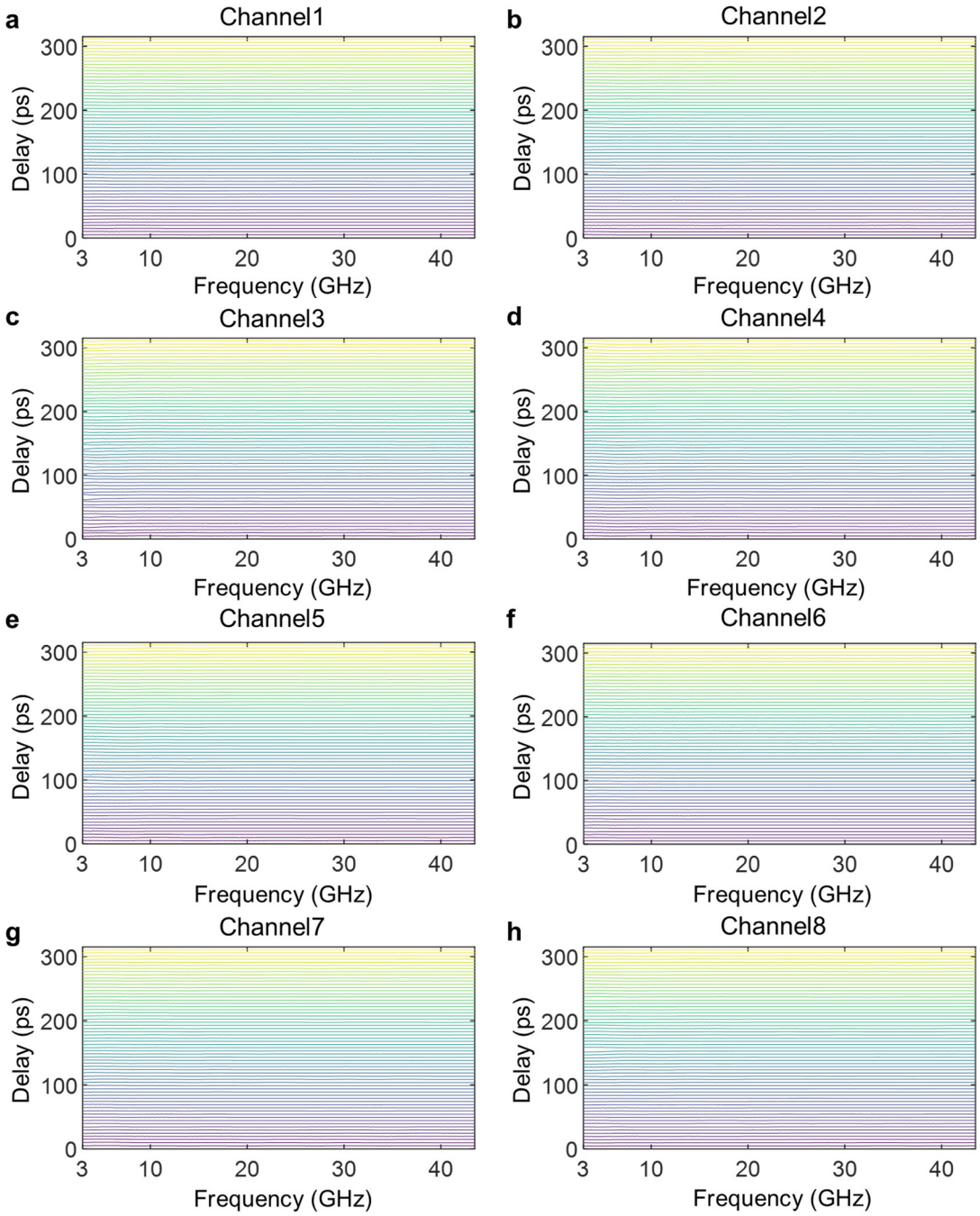

S6. Additional results for beam pattern simulation and experiment

Supplementary Figure 10 presents the simulated far-field beam patterns corresponding to beam steering angles of 7.4°, 14.8°, and 30.8°, evaluated at four representative operating frequencies: 5 GHz, 10 GHz, 20 GHz, and 30 GHz. The simulations are based on the experimentally characterized delay states of the OTTDL chip; the complete set of measured delay values across all 8 optical channels and their 64 reconfigurable delay states was used as input to the beamforming model. The beamforming simulations assume a linear antenna array with 8 elements and a center frequency of 13 GHz. To generate these simulated radiation patterns, we modeled the array factor $AF(\theta)$ as

$$AF(\theta) = \sum_{n=0}^{N-1} e^{j(n\cdot\beta d sin\theta - 2\pi f\cdot\tau_n)} \quad (10)$$

where $\beta=2\pi f/c$ is the wavenumber, d is the inter-element spacing, and τ_n denotes the measured time delay applied to the n-th antenna element. The first term in the exponent accounts for the geometric phase difference due to the incident angle θ, while the second term introduces a programmable phase shift arising from the true-time delay lines. The far-field radiation intensity pattern is then derived from the normalized magnitude of the array factor, expressed in decibels as $20\log_{10}|AF(\theta)|$. This formula enables high-fidelity simulations of frequency-invariant beam steering by incorporating the experimentally measured, frequency-independent time-delay profiles of the OTTDL chip. The results indicate that, for each steering angle, the main lobe direction of the beam remains fixed across all four frequencies. This frequency-invariant beam pointing confirms the true-time delay operation of the chip, enabling beam steering without beam squint—a well-known limitation in conventional phase-shift-based beamforming systems. In addition, the simulations reveal that the beamwidth narrows at higher frequencies due to the shorter wavelength of the signal, which leads to a reduced diffraction limit for the antenna array. As a result, higher frequencies offer improved angular resolution. However, this also leads to the appearance of more pronounced sidelobes, especially at 20 GHz and 30 GHz, which is a typical phenomenon in finite-sized arrays at high frequencies. As the inter-element spacing approaches or exceeds half the wavelength at higher frequencies, the array geometry becomes more prone to the formation of grating lobes, which can significantly elevate sidelobe levels.

Supplementary Fig. 10| Simulated beam patterns at 5, 10, 20, 30 GHz. a 7.4°. b 14.8°. c 30.8°.

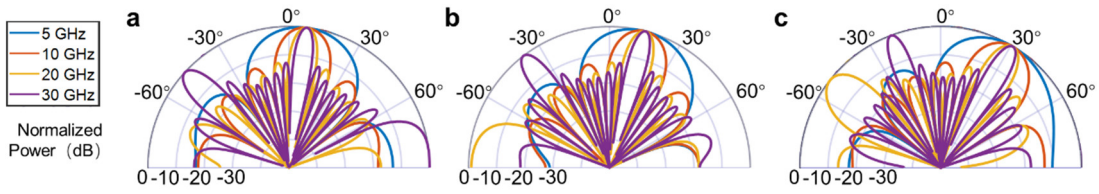

Supplementary Figure 11 presents the experimentally measured far-field beam patterns corresponding to six steering angles (±14.8°, ±30.8°, and ±39.8°), over the frequency range of 12.4 -13.6 GHz with a resolution of 0.1 GHz. The measurements were conducted using a one-dimensional linear antenna array comprising 8 elements, operating at a center frequency of 13 GHz. For each steering angle, the corresponding inter-channel time delays were configured as follows: ± 14.8°: 2×4.93 ps; ±30.8°: ±4×4.93 ps; ±39.8°: ±5×4.93 ps, derived based on array geometry and desired steering directions. As summarized in Supplementary Table 1, the actual beam pointing angles exhibited small deviations from the theoretical ones, with measured values of +15.3 °, -16.2 °, +32.4 °, -29.7 ° and ± 38.7 ° at the corresponding configurations. The 3 dB beamwidths ranged from 12.5° to 16.2°, while the main-to-sidelobe ratios (MSRs) varied between 3.95 dB and 10.67 dB. A gradual degradation in beam quality at larger steering angles is observed, primarily due to delay quantization and aperture truncation effects. Across the 1.2 GHz operational bandwidth, the main lobe consistently tracks the intended angle with minimal frequency dependence, confirming robust and broadband beam steering. The bandwidth limitation is attributed mainly to the antenna gain roll-off rather than the optical delay system, suggesting the feasibility of extending the system bandwidth with optimized RF front-end design.

Supplementary Fig. 11| Measured beam patterns at the steering angles of ±14.8°, ±30.8° and ±39.8° at 12.4-13.6 GHz.

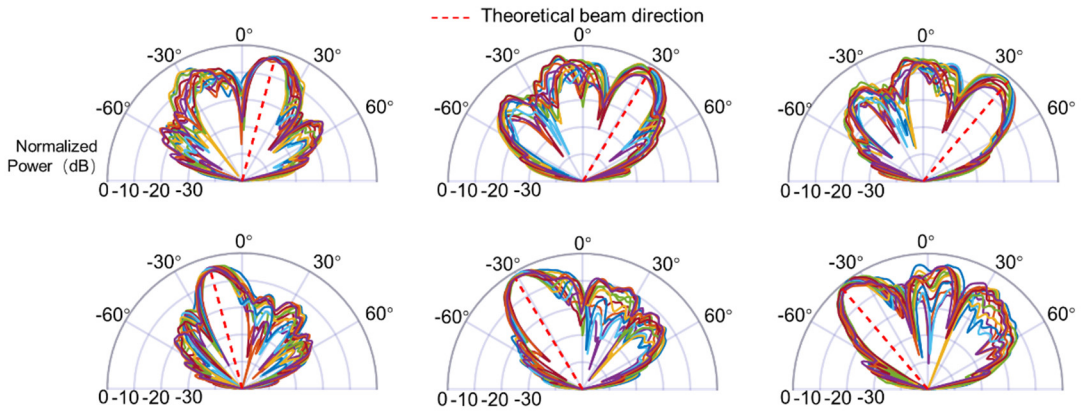

Supplementary Table 1| Simulated and measured beam performance at the steering angles of ±14.8°, ±30.8° and ±39.8° at 13 GHz.

Inter-channel delay difference	Theoretical beam pointing angle	Actual beam pointing angle	Theoretical 3dB beamwidth	Actual 3dB beamwidth	Theoretical MSR	Actual MSR
+2×4.93ps	+14.8°	+15.3°	15.0°	14.4°	13.26dB	7.12dB
-2×4.93ps	-14.8°	-16.2°	15.0°	12.5°	13.26dB	10.67dB
+4×4.93ps	+30.8°	+32.4°	16.9°	16.2°	13.26dB	4.24dB

-4×4.93ps	-30.8°	-29.7°	16.9°	16.2°	13.26dB	10.33dB
+5×4.93ps	+39.8°	+38.7°	18.9°	15.3°	13.26dB	3.95dB
-5×4.93ps	-39.8°	-38.7°	18.9°	14.4°	13.26dB	9.20dB